



Pergamon

Acta Materialia 50 (2002) 5005–5020



www.actamat-journals.com

# Deformation twinning in nanocrystalline Al by molecular-dynamics simulation

V. Yamakov<sup>a</sup>, D. Wolf<sup>a</sup>, S.R. Phillpot<sup>a</sup>, H. Gleiter<sup>b</sup>

<sup>a</sup> Materials Science Division, Argonne National Laboratory, Building 212, 9700 South Cass Avenue, Argonne, IL 60439, USA

<sup>b</sup> Forschungszentrum Karlsruhe, 76021 Karlsruhe, Germany

Received 23 January 2002; received in revised form 17 July 2002; accepted 24 July 2002

## Abstract

We use a recently developed, massively parallel molecular-dynamics code for the simulation of polycrystal plasticity to elucidate the intricate interplay between dislocation and GB processes during room-temperature plastic deformation of model nanocrystalline-Al microstructures. Our simulations reveal that under relatively high stresses (of 2.5 GPa) and large plastic strains (of ~12%), extensive deformation twinning takes place, in addition to deformation by the conventional dislocation-slip mechanism. Both heterogeneous and homogeneous nucleation of deformation twins is observed. The heterogeneous mechanism involves the successive emission of Shockley partials from the grain boundaries onto neighboring slip planes. By contrast, the homogeneous process takes place in the grain interiors, by a nucleation mechanism involving the dynamical overlap of the stacking faults of intrinsically and/or extrinsically dissociated dislocations. Our simulations also reveal the mechanism for the formation of a new grain, via an intricate interplay between deformation twinning and dislocation nucleation from the grain boundaries during the deformation. The propensity for deformation twinning observed in our simulations is surprising, given that the process has never been observed in coarse-grained Al and that the well-known pole mechanism cannot operate for such a small grain size. It therefore appears that the basic models for deformation twinning should be extended with particular emphasis on the role of grain-boundary sources in nanocrystalline materials.

© 2002 Published by Elsevier Science Ltd on behalf of Acta Materialia Inc.

**Keywords:** Computer simulation; Nanocrystal; Aluminium; Deformation twinning; Dislocations

## 1. Introduction

In polycrystalline materials the process of deformation twinning often competes with slip deformation at low temperature [1]. The activated twin systems, usually different from the slip systems, enrich the possibilities of the material to respond to external load. Twinning therefore enhances the ductility in structures with a relatively small number of slip systems, such as hcp crystals. However,

twinning is also observed in crystals of higher symmetry, such as bcc and some fcc metals. The low stacking-fault energy of some materials also favors deformation twinning [2].

Experimental studies on coarse-grained fcc metals, such as Cu, Ni and Al, reveal no evidence for twinning under normal conditions [3]. Generally, the absence of deformation twinning in fcc metals may be due to one or a combination of the following causes. (i) Experiments reveal that twinning

takes place at much higher stresses than slip deformation [3] (by more than an order of magnitude higher); (ii) the existence of a large number of slip systems in the fcc structure makes slip a very efficient deformation mechanism; and (iii) the common pole mechanism for twinning [4], usually observed in bcc crystals, is more complicated in fcc structures because the twinning direction is different from the slip direction [5].

These observations indicate that deformation twinning in fcc metals takes place only after sufficient strain hardening has occurred to create high stress concentrations. [3] This can be achieved by deformation conditions where recovery is suppressed, requiring either a very low deformation temperature or a high strain rate. For example, the pioneering experiment of Blewitt et al. [6] on Cu revealed twinning at 4.2 K and 77.3 K, respectively, after about 50 and 75% slip-induced strain. Twinning has also been observed during quasi-static, high strain-rate ( $\sim 10^3 \text{ s}^{-1}$ ) compression of Cu and Cu-Al alloys [2]. Also, shock loading of Al-Mg alloys to 13 GPa at  $-180^\circ\text{C}$  has been observed to induce twinning [7], although in pure Al with a grain size of  $150 \mu\text{m}$ , no twinning takes place under the same conditions.

Deformation twinning becomes even more difficult as the grain-size,  $d$ , decreases towards  $\mu\text{m}$  dimensions. A theoretical analysis of the deformation solely due to the pole mechanism for twinning in fcc metals [8,9], i.e., in the absence of any dislocation substructure in the vicinity of the pole source, shows that the required twinning stress,  $\sigma_t$ , for the source to operate is inversely proportional to the size of the source ( $\sigma_t \sim d^{-1}$ ) [9]. However, when the interactions among the dislocations piling up against the twin boundary created from the pole source are taken into account, the usual Hall-Petch dependence ( $\sigma_t \sim d^{-1/2}$ ) is obtained [9].

In a recent experimental study on the grain-size dependence of twinning in polycrystalline 70/30 brass and MP35N alloy (a multiphase Co-Ni-Cr-Mo alloy), El-Danaf et al. [10] observed a power-law increase of  $\sigma_t$  with decreasing grain size between  $300 \mu\text{m}$  and  $30 \mu\text{m}$  ( $\sigma_t \sim d^{-k}$ , with  $k = 0.89$ ); no twinning was observed at the smaller grain sizes of  $7$  and  $1 \mu\text{m}$  for the MP35N alloy

[10]. To interpret these observations, these authors proposed that deformation twinning in polycrystalline fcc metals is controlled by the homogeneous slip length,  $L$ , which in turn is governed by the dislocation density on the slip plane, leading to the empirical expression [10]

$$(\sigma_t - \sigma_0)/G = C \left( \frac{L}{b} \right)^{-k}. \quad (1)$$

Here  $\sigma_0$  is the initial yield strength (i.e., prior to the onset of twinning),  $G$  is the shear modulus,  $b$  is the Burgers vector of the twin dislocations and  $C$  ( $= 0.0004$ ) and  $k$  ( $= 0.89$ ) are dimensionless fitting parameters [10].

According to Eq. (1), a decreasing grain size has two effects on the propensity for twinning. First, due to the usual Hall-Petch hardening the ‘background’ yield stress,  $\sigma_0 = Ad^{-1/2}$ , which has to be overcome for twinning to occur, increases with decreasing grain size. Second, since in the limit of small grain size dislocations cannot traverse the grain boundaries (GBs),  $L = d$ . Eq. (1) therefore yields:

$$\sigma_t / G = Ad^{1/2} / G + C \left( \frac{d}{b} \right)^{-k}. \quad (2)$$

The overall effect is the observed termination of twinning below a certain relatively small grain size [10].

Computer simulations on shear-induced twinning have so far been limited to single crystals [11–13]. For example, Hu et al. [11] used molecular-statics simulations to study the stress-strain curve of  $\alpha$ -Fe single crystals under uniaxial tensile deformation, yielding insight into the atomic structure of the observed deformation twins. Also, Pinsok and Ackland [12] used molecular-dynamics (MD) simulations to apply shear to an already twinned microstructure of hcp Zr; they observed production of partial dislocations as a result of the twin elimination during the process of recovery, accompanied by the formation of energy-stabilized fcc nanocrystals. Finally, the MD simulations of Lill and Broughton [13] revealed the process of twinning in connection with martensitic transformations.

Given the experimental observations on coarse-

grained materials and the understanding of the process as captured, for example, in Eqs. (1) and (2), twinning appears very unlikely to contribute to the deformation of nanocrystalline materials (i.e., polycrystalline materials with a grain size of typically less than  $0.1\ \mu\text{m}$ ). It is therefore not surprising that, to date, the possibility for deformation twinning in nanocrystalline metals remains entirely unexplored, either by simulation or experiment. In the present paper we use a recently developed, massively parallel MD code for the simulation of polycrystal plasticity [14,15] to elucidate the intricate interplay between dislocation and GB processes during room-temperature plastic deformation of model nanocrystalline-Al microstructures. Our simulations reveal that under relatively large plastic strains (of  $\sim 12\%$ ), deformation twinning takes place in addition to deformation by the conventional dislocation-slip mechanism. Moreover, we identify the atomic-level mechanism by which a microtwin nucleated from the GBs serves as the nucleus for the formation of a new grain, suggesting that deformation twinning can be a mechanism for triggering dynamical recrystallization. These simulations suggest that a reexamination of the basic models for twinning, with particular emphasis on a nanometer grain size, may be timely.

The paper is organized as follows. Our simulation approach is briefly summarized in Section 2. In Section 3 our simulation results on the nucleation of deformation twins are presented and the observed nucleation mechanisms are analyzed. The atomic structure and dynamic properties of several types of incoherent twin boundaries observed in our simulations are analyzed in Section 4. In Section 5 we discuss the reasons why, in our view, deformation twinning should, in fact, be expected to play a significant role in the deformation of nanocrystalline fcc metals.

## 2. Simulation approach and background

We have recently developed an approach for the simulation of dislocation processes in nanocrystalline fcc metals. [14,15] In the first application of the new approach,  $[1\bar{1}0]$  textured (or columnar)

polycrystalline microstructures with full three-dimensionally (3d) periodic border conditions of the Parrinello-Rahman type [16] were investigated. While providing a fully 3d treatment of the underlying physics, the GB and dislocation events taking place during the deformation are readily visualized in such a microstructure. Also, it enables us to simulate relatively large grains because only a few (in our case 10)  $(1\bar{1}0)$  lattice planes need to be considered in the periodically repeated texture ( $z$ ) direction.

In these [14,15] and the present simulations, idealized microstructures consisting of four grains of identical size and regular-hexagonal shape were considered (see Fig. 1). The grains were oriented relative to the edge of the simulation cell (the  $X$  axis) by rotations about  $[110]$  by the angles  $0^\circ$ ,  $30^\circ$ ,  $60^\circ$  and  $90^\circ$  (see Fig. 1). As a consequence, all the GBs in the simulation cell are asymmetric high-

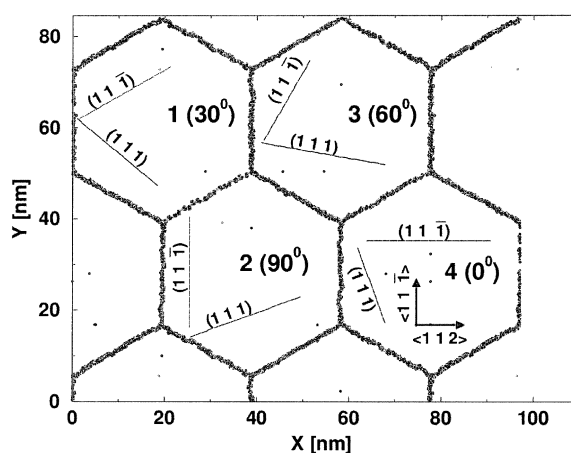


Fig. 1. Orientations of the four grains relative to the edge of the simulation cell ( $X$  direction, corresponding to the  $\langle 112 \rangle$  direction in grain 4; i.e., the misorientation angle of each grain is given by the angle between its  $\langle 112 \rangle$  direction and the  $X$  axis). The orientations are mapped onto a  $[110]$ -projected snapshot of the system with a grain size of  $d = 45\ \text{nm}$  after its thermal equilibration at  $T = 300\ \text{K}$  but prior to application of external stress. Also indicated are the orientations of the two sets of  $\{111\}$  slip planes in each grain. Only atoms with nearest-neighbor coordination deviating from the fcc perfect-crystal value of 12 are shown. The continuous network of these miscoordinated atoms tracing the GBs indicates that all these  $[110]$  tilt GBs are high-angle GBs. The GBs remain perfectly straight until the threshold stress for the nucleation of dislocations is reached.

angle  $[1\bar{1}0]$  tilt boundaries. The continuous lines of defected GB atoms in Fig. 1 indicate that the GBs are, indeed, high-angle GBs. The  $[1\bar{1}0]$  column axis ensures that, following their nucleation, dislocations can glide in each grain on either of two  $(111)$  or  $(1\bar{1}\bar{1})$  slip systems, unimpeded by the 3d-periodic border conditions imposed on the simulation cell (for details, see Ref. [14]).

An EAM potential parameterized for Al [17] is used throughout this study. This potential was fitted to give the correct zero-temperature lattice constant ( $a_0 = 4.03 \text{ \AA}$ ), elastic constants,  $(111)$  intrinsic stacking-fault and surface energy, cohesive energy and vacancy formation energy. The potential has been slightly modified for a higher degree of smoothness at the cut-off radius. This cut-off modification increases the stacking-fault energy from  $104 \text{ mJ/m}^2$  to  $122 \text{ mJ/m}^2$ , i.e., closer to the experimental values, ranging between  $120$  and  $142 \text{ mJ/m}^2$  [18].

MD simulations were carried out under constant tensile loads of  $2.3$  and  $2.5 \text{ GPa}$  and at a temperature of  $T = 300 \text{ K}$  (the melting point,  $T_m$ , for this potential was estimated at about  $940 \text{ K}$  [17]). As in various previous simulations [14,15,19–21], common-neighbor analysis [22,23] will be used to visualize the presence of stacking faults in the structure. Being able to identify atoms in local hcp and fcc environments, this analysis permits the distinction between various types of planar stacking disorder. For example, in a columnar microstructure a single line of hcp atoms identifies a coherent twin boundary, while two adjacent hcp lines indicate an intrinsic stacking fault (ISF); two hcp-coordinated lines of atoms with an fcc line of atoms between them represents an extrinsic stacking fault (ESF) (see also Figs. 2 and 3 below).

Using this simulation model, our previous work [14] revealed the onset of plastic flow in nanocrystalline Al when the applied tensile stress exceeds the threshold stress (of about  $2.3 \text{ GPa}$ ) for the nucleation of extended  $1/2[011]$  dislocations from the GBs or grain junctions. The nucleation mechanism involves the successive emission of both the leading  $1/6[112]$  and trailing  $1/6[\bar{1}21]$  Shockley partials connected by a stacking fault. Following their complete nucleation, these dislocations travel across the grains on one of the available  $\{111\}$  slip

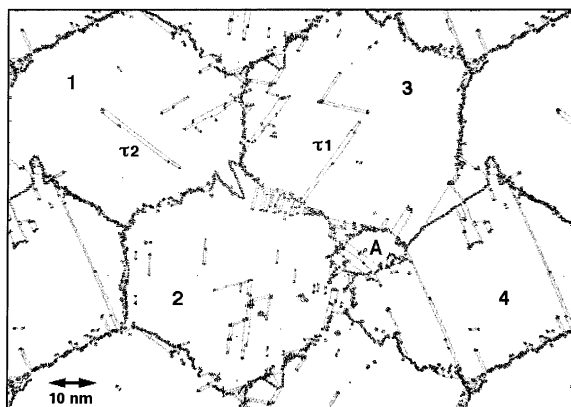


Fig. 2. Snapshot at 11.9% plastic strain for the structure in Fig. 1 (i.e., with  $d = 45 \text{ nm}$ ). A variety of processes involving dislocation-dislocation and dislocation-GB interactions are shown to take place. Formations  $\tau_1$  and  $\tau_2$  mark, respectively, heterogeneously and homogeneously nucleated deformation twins in grains 3 and 1. Formation of a new grain, labeled A, is also seen. Here and throughout, common-neighbor analysis was used to identify perfect-crystal atoms as being either in a local hcp (gray atoms) or fcc environment (atoms not shown). Black atoms are 'defected', i.e., neither in an fcc nor hcp environment, including atoms not having 12 nearest neighbors. (A movie of the full simulation is posted at the supplementary information to ref. [15] as well as at [www.msd.anl.gov/groups/im/movies/deform.html](http://www.msd.anl.gov/groups/im/movies/deform.html)).

planes, until annihilated in another GB. Below this critical stress, the system deforms very slowly via a GB-based mechanism which renders the network of straight, sharp GBs virtually unchanged during the deformation.

The magnitude of the splitting distance of the dissociated dislocations in the presence of the applied stress introduces an important length scale into the system. [14] The length-scale competition between this splitting distance and the grain size plays a critical role in the deformation of nanocrystalline materials. In particular, if the grain is not large enough to enable the nucleation of both partials required to form a complete dislocation, the dislocation-slip mechanism ceases to be operational [14] in favor of a GB-based deformation mechanism [24]. This explains the results of previous simulations on systems with a rather small grain size ( $d < 12 \text{ nm}$ ) [19–21], in which dislocation activity consisted only of the emission of individual Shockley partials, i.e., of incomplete

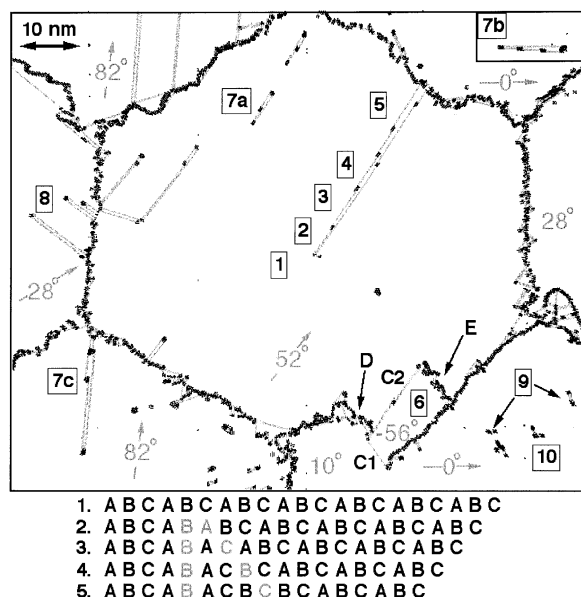


Fig. 3. Snapshot of grain 3 for a grain diameter of 70 nm at 10.3% plastic strain, revealing several known mechanisms involved in the formation of deformation twins (seen in (1–5), (6), and (7a–c), respectively; (for details, see the text). We note that configuration 7b shown as an inset was taken from a different region of the sample. The ... ABCABC ... stacking sequences of the three types of (111) planes in the face centered cubic (f.c.c.) lattice, labeled A, B and C, in five regions of the twinned grain are indicated in the schematic at the bottom of the figure. Letters in gray, denoting those having the same neighbours on both sides, indicate planes in a hexagonal close-packed (h.c.p) ... ABAB ... (or ... ACAC ... or ... BCBC ...) stacking sequence. (8) indicates the process of nucleation of double-Shockley partials, leaving behind extrinsic stacking faults. (9) points to two dissociated into partials extended dislocations while (10) represents a Lomer-Cottrell lock. A comparison of the orientations of different regions relative to the  $X$  axis with those in the undeformed microstructure (see Fig. 1) indicate that significant rotations about [110] have taken place during the deformation.

dislocations still attached to the GBs. It was found that in this case dislocations do not significantly contribute to the deformation.

We finally note that the resolved shear stresses in these [14,15] and the present simulations, of the order of 1 GPa on the {111} slip planes of our system, are well below the theoretical shear strength,  $\sigma_{th}$ , for Al. Frenkel's perfect-crystal shear model [25] gives an estimate of  $\sigma_{th} = G/2\pi$ ; with  $G = 32.5$  GPa for Al at OK (to which our potential was fitted [17]), we obtain a value of  $\sigma_{th} = 5.18$

GPa at OK, and slightly lower at room temperature. This range of values is in good agreement with recent nanoindentation experiments on Al thin films which yielded values of  $\sigma_{th}$  in the range of 4.2–4.5 GPa, leading the authors to conclude that the Frenkel formula is well satisfied for Al [26,27].

### 3. Mechanisms for deformation twinning

As described above, our previous simulations revealed the onset of plastic flow when the applied stress exceeds the threshold stress for the nucleation of extended dislocations from the GBs and grain junctions. As the plastic strain increases with time, the dislocation concentration in the grain interiors increases rapidly, due to the continuously increasing nucleation activity at the GBs under the constant applied tensile load [14]. This enhancement of the dislocation-nucleation rate is a direct consequence of the rapidly developing roughness of the initially flat GBs, as they emit and absorb ever larger numbers of dislocations. While, by comparison with experiments, this aspect of our simulations may be somewhat unrealistic, it provides the opportunity to investigate the mechanisms of a variety of dislocation-GB interaction processes which take place only after substantial deformation has occurred and under high stresses, i.e., in a deformation regime in which dislocation-dislocation and dislocation-GB interaction processes compete on an equal footing.

Fig. 2 shows a snapshot of a deformation substructure thus obtained after 11.9% plastic straining at strain rate of  $2 \times 10^8 \text{ s}^{-1}$  of a sample with a grain size of 45 nm [14]. The high dislocation concentration in this snapshot (of about  $10^{15} \text{ m}^{-2}$ ) reveals various types of intragranular dislocation-dislocation interaction processes associated with the glide of extended dislocations on different slip systems. Most of these processes are well-known from extensive deformation studies in single crystals and coarse-grained polycrystals [28–31]. Among the best known is the formation of Lomer-Cottrell locks [29,30], seen in each of the four grains in Fig. 2. The detailed dynamics of Lomer-Cottrell lock formation in our simulation are revealed in the movie described in the figure caption.

Fig. 2 also reveals that the slip-deformation process in our nanocrystalline model system is accompanied by extensive deformation twinning. It is well-known that, by analogy with a phase transformation [1], the process of deformation twinning requires first the nucleation of a small microtwin which subsequently grows to enlarge the new grain thus formed. The existence of a twin interface with positive excess energy strengthens this analogy as it represents a nucleation barrier. It is also well established that this nucleation can happen either heterogeneously (i.e., from a suitable defect in the crystal lattice, such as a GB) or homogeneously (i.e., in the grain interiors, at a certain point in the near-perfect crystal lattice where the stress concentration exceeds a critical level). A detailed analysis of the deformation kinetics leading to Fig. 2 (see also our movie) reveals that two distinct types of twinning processes (labeled  $\tau_1$  and  $\tau_2$  in the figure) have, indeed, taken place; the first nucleus, labeled  $\tau_1$ , was formed *heterogeneously* from a GB, whereas the second, labeled  $\tau_2$ , was formed *homogeneously* in the grain interior. In the following two subsections, these two processes will be discussed in detail; they are followed by a description of how these nuclei can grow to form a new grain.

### 3.1. Heterogeneous nucleation of a twin lamella from the GBs

The regions labeled (1) through (5) in Fig. 3 characterize the formation and early stages of growth of a twin lamella nucleated heterogeneously from a GB. The twinning takes place by emission from the GB of successive  $1/6[112]$  edge partial dislocations on adjacent  $(11\bar{1})$  planes [1,28,29]. These partial dislocations are the so-called twinning dislocations in the fcc lattice; they successively shift the  $(11\bar{1})$  stacking planes in a manner shown in the schematic at the bottom of the figure, giving rise to the formation of a new grain. The detailed twinning mechanism involves the following five regions defined in Fig. 3: 1. perfect fcc crystal; 2. ISF; 3. ESF; 4. two coherent twin boundaries separated by two  $(11\bar{1})$  planes, and 5. more widely separated twins.

A second, entirely different mechanism for twin

formation is seen in region 6 in Fig. 3. This mechanism, proposed by Ashby and Harper [32] and also described by Gleiter [33], involves the splitting and subsequent migration of a GB segment, leaving behind two coherent twin boundaries (C1) and (C2) (marked as single gray lines of hcp atoms). The process takes place via the dissociation of the initial GB segment (D) into a twin boundary (C1) and a *new* GB (E). The twin boundary (C1) remains fixed at the initial position of (D) before the dissociation, while the migration of the new GB (E) produces the twin lamella (6) separated by the second twin boundary (C2) from the non-twinned crystal lattice of the grain. Fullman and Fisher [34–36] have suggested that this process is driven by a lowering of the crystal energy.

Several other interesting events are seen in Fig. 3. For example, region 8 reveals the process of nucleation of D-Shockley partials, leaving behind ESFs. This process has been observed before in fully 3d microstructure simulations for Cu by Schiotz et al. [20]. The two configurations, labeled 9, represent extended dislocations dissociated into partials while gliding along the  $(111)$  and  $(11\bar{1})$  glide planes; eventually two such dislocations can form a Lomer-Cottrell lock, such as the one seen in 10.

A comparison of the orientations of different crystal regions relative to the X axis shown in Fig. 3 with those in the undeformed microstructure (see Fig. 1) indicate that significant grain rotations about  $[1\bar{1}0]$  have taken place during the deformation. The high degree of non-uniformity of these rotations, particularly in the vicinity of the lamellar twin in configuration 6, is noteworthy. However, these orientations confirm the near  $70.5^\circ$  and  $180^\circ - 70.5^\circ = 109.5^\circ[1\bar{1}0]$  tilt misorientations across the different twin boundaries in configuration 6.

The need for some kind of extended defect configuration, such as GBs and grain junctions, renders the mechanisms of heterogeneous nucleation less common in coarse-grained than nanocrystalline materials. In coarse-grained materials twinning dislocations move from one glide plane to the next via the well-known pole mechanism [8,9]. Although in nanocrystalline materials the pole mechanism cannot operate (because of the high

twinning stress associated with the small grain size [9]), our simulations suggest that the high GB density provides plentiful sources for the nucleation of twinning dislocations, albeit only at elevated stresses.

### 3.2. Homogeneous nucleation of twin lamellae from the grain interior

As seen in Fig. 3, twin nucleation can also take place by a homogeneous process. When the Shockley partials of two extended dislocations on neighboring planes glide past one-another, the ISFs of the two dislocations in the region of overlap combine to form an ESF (formation 7a in Fig. 3; for atomic-level details, see Sec. 4). This process can proceed further. For example, when a third extended dislocation joins the overlapped pair, an ESF configuration, such as that captured in 7a, transforms into a two-layer microtwin (formation 7b in the inset to Fig. 3). Alternatively, when two *extrinsically* dissociated dislocations, i.e., extended dislocations terminated by two *double-Shockley* (D-Shockley) partials and connected by an ESF [37], overlap (formation 7c in Fig. 3), a three-layer microtwin is formed. All these processes involving the overlap of different stacking faults result in the formation of a twin lamella of the type known as a lenticular twin [1]. A fully nucleated twin of this type is seen in Fig. 2 (configuration  $\tau_2$  in grain 1).

As an example, the dislocation kinetics leading to this configuration ( $\tau_2$ ) is revealed by the four snapshots in Fig. 4(a–d). The nucleation starts at the *extrinsically* dissociated dislocation, d1, in (a), which is pinned at a sessile dislocation produced by a previous reaction between two dislocations that crossed each-other (not shown). Proceeding to (b), the dislocation has extended under the applied stress while an *intrinsically* dissociated dislocation, d2, approaches; the latter was nucleated from the GB on a neighboring (111) plane. In (c), the *intrinsic* stacking fault of d2 overlaps with the *extrinsic* stacking fault of d1, thus forming the twin nucleus,  $\tau_2$ . Finally, as seen in (d), this nucleus subsequently lengthens by glide of the partial dislocations initially forming d1 and d2. At that point these partials are called the ‘twinning dislocations’ of the lenticular twin [1].

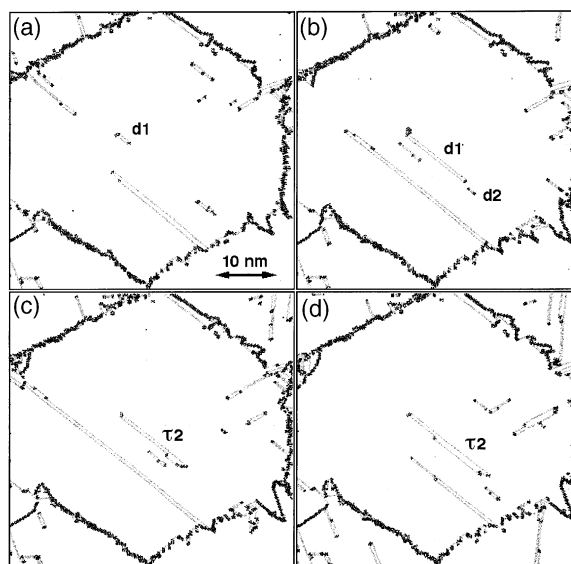


Fig. 4. Successive snapshots taken at 2 ps time intervals, revealing the mechanism for the homogeneous nucleation of the lenticular twin,  $\tau_2$ , inside grain 1 in Fig. 2. The mechanism starts at the pinned, *extrinsically* dissociated dislocation, d1, in (a). As seen in (b), while this pinned dislocation lengthens under the effect of the applied stress, it overlaps with an incoming, *intrinsically* dissociated dislocation, d2, thus forming the twin nucleus,  $\tau_2$ , seen in (c) and (d).

In addition to this mechanism of stacking-fault overlap (configurations  $\tau_2$  in Fig. 4(c) and (d) and 7a in Fig. 3), our simulations reveal the nucleation of *extrinsically* dissociated dislocations directly from the GBs. The first step in this nucleation is seen in region 8 in Fig. 3, showing D-Shockley partials trailed by ESFs (seen also in ref. 20). The complete nucleation of an *extrinsically* dissociated dislocation requires emission of a second D-Shockley partial from the same GB. Instead, however, as revealed by the snapshots of a complete nucleation event in Fig. 5, the emission of a D-Shockley partial in (a) is followed by the emission of a *single*-Shockley partial, transforming the tail of the *extrinsic* stacking fault into an *intrinsic* stacking fault. (c) reveals that this trailing ISF has been cut in two. The part closest to the GB is subsequently re-absorbed into the GB; by contrast, the other part gets absorbed into the *extrinsically* dissociated dislocation while converting its two partials into the D-Shockley partial trailing the now complete,

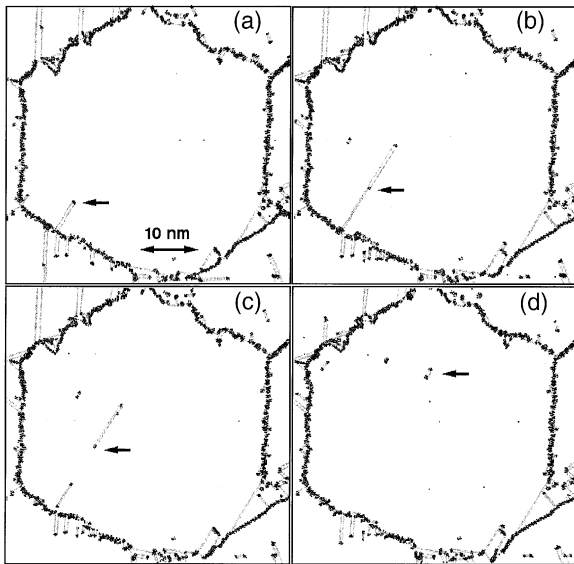


Fig. 5. Successive snapshots taken at 3 ps time intervals, revealing the mechanism for the nucleation of an *extrinsically* dissociated dislocation in grain 3. As indicated by the arrow, (a) shows the emission from the GB of a D-Shockley partial trailed by an extrinsic stacking fault. In (b), a single-Shockley partial is emitted, transforming the *extrinsic* into an *intrinsic* stacking fault. c) reveals that the intrinsic stacking fault has been cut in two, and that the part closest to the GB is being re-absorbed into the GB. Finally, comparison of (c) and (d) reveals that this complex dislocation, containing regions of both ESF and ISF, is being converted into the complete, *extrinsically* dissociated dislocation seen in (d).

*extrinsically* dissociated dislocation (compare (c) and (d)).

The dislocation structures of the various types of extrinsically dissociated dislocations observed in our simulations are in complete agreement with those determined in the MD simulations of Al single crystals by Hirth and Hoagland [37]. In particular, they showed that each D-Shockley partial is composed of two S-Shockley partials of different types. An extrinsically dissociated dislocation therefore consists of four elementary S-Shockley partials and an ESF; the various combinations between these four can form different types of extrinsically dissociated dislocations [37].

The growth of a lenticular twin involves both lengthening and broadening of a previously nucleated twin lamella [1]. Our simulations reveal that the twin lengthens by increasing the dis-

sociation distance of the twinning dislocations already in their structure, via glide of their cores along the glide planes (see also Fig. 4(c) and (d)). The twin broadens by a mechanism similar to the nucleation process, by absorbing other extended dislocations from neighboring planes, thus forming additional twinning dislocations.

We mention that, by contrast with our columnar microstructure, in a fully 3d microstructure a lenticular twin is formed by a series of *loops* of twinning dislocations [1], rather than individual cores. While its lengthening involves the expansion of these loops, its broadening during growth occurs via incorporation of other dislocation loops by overlap processes analogous to the ones observed above.

The elementary mechanism of intrinsic stacking-fault overlap transforms two hcp planes (one from each of the two ISFs) into fcc planes, releasing energy approximately equal to the ISF energy. This renders the overlap an energetically favorable mechanism that joins dislocations on neighboring glide planes together. Several such configurations are seen in the vicinity of configuration 7a in Fig. 3. This observation suggests that the formation of lenticular twins by this mechanism is driven energetically, and is able to occur when the concentration of the extended dislocations is rather high. The partials are absorbed by the twin interface, releasing the energy of their stacking faults. Thus twinning may also be considered as the result of the follow-up process of recovery during the deformation.

### 3.3. Growth of a twin lamella to form a new grain

The most intriguing process revealed in Fig. 2 involves the nucleation of the new grain A. The sequence of snapshots shown in Fig. 6 captures in detail the underlying GB and dislocation processes in the vicinity of the triple junction involving grains 2, 3 and 4 (see also Fig. 1).

The nucleation of the new grain (via events (1–5) in Fig. 6) starts by the emission of a complete  $1/2[011]$  dislocation from the GB between grains 3 and 4 (event (1) in (a)). Almost simultaneously another complete dislocation with a  $1/2[101]$  Burg-



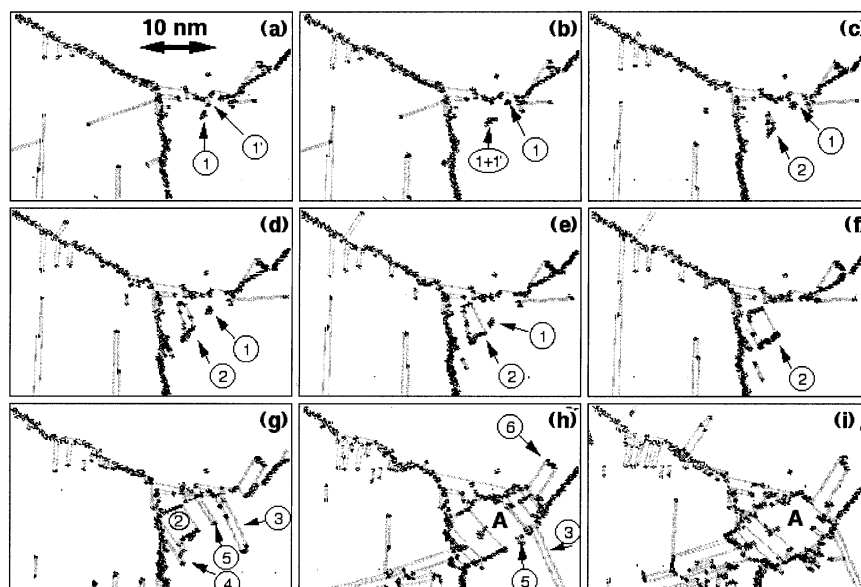


Fig. 6. Successive snapshots of the vicinity of the triple junction connecting grains 2 (lower left), 3 (top) and 4 (lower right) in Fig. 2, demonstrating the mechanism by which the new grain (A) is formed during about 50 ps of simulation time. (a)  $\epsilon=6.03\%$  plastic strain; (b) 6.09%; (c) 6.14%; (d) 6.19%; (e) 6.25%; (f) 6.32%; (g) 6.76%; (h) 8.71% and (i) 10.33%. Several distinct processes are revealed. (1) and (1'): emission of complete dislocations from the GB between grains 3 and 4; (2) formation of a new grain by nucleation of a twin lamella from these dislocations; (3) formation of a glissile twin lamella in grain 4; (4) continuous emission of partials from the GB which join the growing twin by the mechanism of stacking-fault overlap; (5) in (g) and (h) nucleation of an extrinsically dissociated dislocation from the GB; (6) in (h) formation of a sessile twin lamella in grain 3.

ers vector (i.e., on another slip system) is emitted from the same GB (event (1') in Fig. 6(a)). The two dislocations ((1) and (1')) subsequently combine, forming the more complicated core structure seen in (b) (labeled (1+1')). As seen in (c) and (d), this virtually immobile core subsequently begins to continuously emit partials, producing a growing twin lamella (event (2)) by a mechanism known as 'partial-dislocation breakaway' [28]. This lamella grows further by absorbing additional  $1/2[011]$  dislocations emitted from the same GB (event (1) in (c–e)), leading to its increased size in (f). On its other side, towards grain 2 (lower left), the twin lamella grows by slow drift of the leading  $1/2[011]$  dislocation towards grain 2. The process is facilitated by continuous absorption of partials emitted from the GB between grains 2 and 4, which join the growing twin by the mechanism of stacking-fault overlap (process (4) in (g), similar to the processes labeled 7a–7c in Fig. 3).

Proceeding from snapshot (f) to (g) reveals further growth of the nucleus for the new grain. In

(g) we observe emission of another twin lamella (labeled (3)) which quickly propagates through the grain. Process (5) in (g) marks the initiation of an ESF headed by a D-Shockley partial. In (h) this ESF has been terminated by a second D-Shockley partial, now forming an extrinsically dissociated dislocation; this process is similar to the one captured in Fig. 5. The combination of these processes results in the rather complex deformation substructure in grain 4 seen in (g). Finally, in snapshots in (g–i) this substructure coalesces to form the new grain A in Fig. 2.

This mechanism of formation of a new grain from a twin lamella can be considered as a further generalization of the process of segregation of partials by the stacking-fault overlap mechanism of twin nucleation described in the Sec. 3.2. Both processes are driven by the necessity to decrease the excess energy by joining a large number of defects, formed during the deformation (e.g., dislocations, stacking faults, twins, etc.) into a new formation with a lower energy. This suggests the possibility

that formation of microtwins can be viewed as the initial stage of recrystallization under deformation, taking place particularly at very high strain rates.

The atomic-resolution snapshot in Fig. 7 of the configuration in the vicinity of the new grain A in Fig. 2 reveals the lattice rotations that have taken place as a result of the 11.9% plastic straining. Particularly noteworthy is the non-uniformity of the orientations both within the new grain and in its vicinity (see also Fig. 1). We note the near  $70.5^\circ$  and  $109.5^\circ$   $[110]$  misorientations across the twin boundaries in the microstructure.

#### 4. Atomic-level analysis of elementary dislocation mechanisms

The above simulations demonstrated that the mechanisms for the nucleation, growth and motion of deformation twins involve a variety of dislocation reactions between Shockley partials in combination with intrinsically or extrinsically dissociated dislocations. Here we analyze these

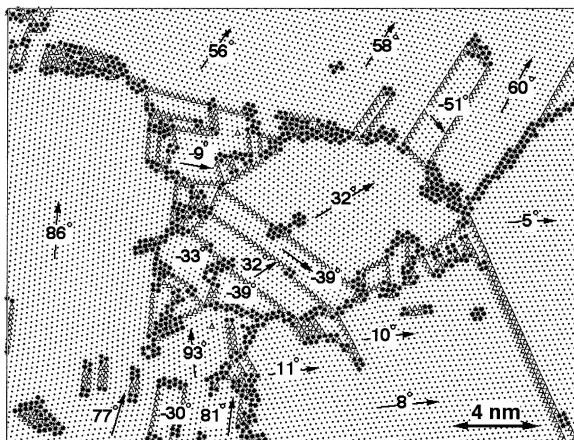


Fig. 7. Atomic-resolution picture of the configuration in the vicinity of the new grain A in Fig. 2 (taken slightly after the snapshot in Fig. 6 (i)). Common-neighbor analysis distinguishes atoms in fcc ( $\cdot$ ), hcp ( $\Delta$ ) and defected ( $\bullet$ ) surroundings. A comparison, with the initial orientations of grains 2, 3 and 4 in Fig. 1 reveals that extensive, highly non-uniform lattice rotations have taken place as a result of the 11.9% deformation. In accordance with the definition of the grain orientations in Fig. 1, the arrows point along  $[112]$  directions.

elementary dislocation mechanisms and reactions in some detail.

To facilitate this atomic-level analysis, we first define some simple terminology and recall the basic crystallography of dissociated dislocations in fcc metals. Our particular columnar simulation geometry restricts the dislocation line to be parallel to the  $[1\bar{1}0]$  direction. The two possible glide planes,  $(111)$  and  $(1\bar{1}\bar{1})$ , combined with two possible glide directions on each, yield four slip systems in each grain. Using Thompson's well-known crystallographic notation [38], Fig. 8 collects for the case of the  $(1\bar{1}\bar{1})$  glide planes the possible decompositions of complete dislocations in our system into partials.

Three types of intrinsically dissociated dislocations can exist on the  $(1\bar{1}\bar{1})$  plane (see Fig. 8): (a) the  $60^\circ$   $1/2[101]$  dislocation, labeled DA, which

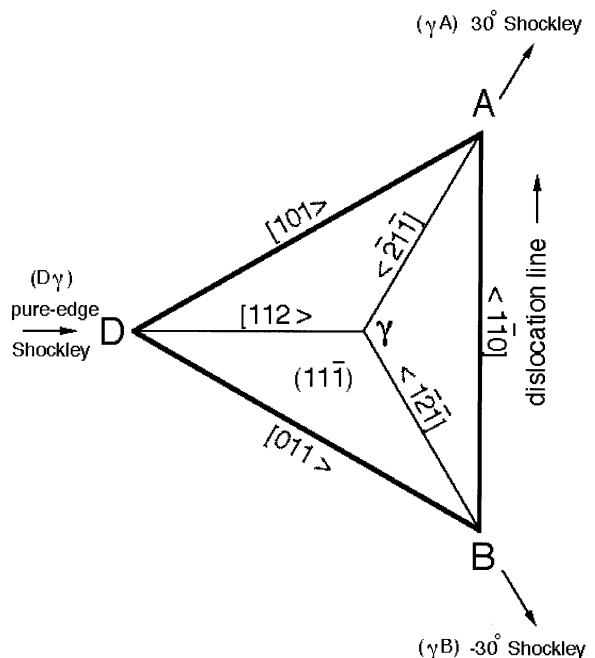


Fig. 8. Thompson notation [38] for the dislocation dissociation reactions possible on the  $(1\bar{1}\bar{1})$  glide plane of our columnar fcc microstructure, in which the dislocation line is fixed to be parallel to  $\langle 1\bar{1}0 \rangle$ . BA, DB and DA indicate complete dislocations (with Burgers vectors  $1\bar{1}0$ ,  $011$  and  $101$ , respectively). These can dissociate into combinations of Shockley partials labeled  $\gamma B$  (a mixed,  $-30^\circ$  partial with Burgers vector  $\langle 1\bar{2}\bar{1} \rangle$ ),  $D\gamma$  (a pure-edge,  $[112]$  partial) and  $\gamma A$  (a mixed,  $30^\circ$   $\langle 2\bar{1}\bar{1} \rangle$  partial).

dissociates into a pure-edge  $1/6[112]$  partial, labeled  $D\gamma$ , combined with a  $30^\circ$   $1/6[2\bar{1}1]$  partial, labeled  $\gamma A$ ; (b) the  $-60^\circ$   $1/2[011]$  dislocation, DB, which dissociates into a pure-edge  $1/6[112]$  partial,  $D\gamma$ , and a  $-30^\circ$   $1/6[\bar{1}21]$  partial,  $\gamma B$ ; and (c) a pure-screw  $1/2[1\bar{1}0]$  dislocation, BA, which dissociates into a  $-30^\circ$   $1/6[1\bar{2}\bar{1}]$  partial,  $B\gamma$ , and a  $30^\circ$   $1/6[2\bar{1}1]$  partial,  $\gamma A$ . These dissociation reactions can be written as (see Fig. 8):



The three glide directions on the  $(11\bar{1})$  plane are therefore  $[011]$ ,  $[101]$  and  $[\bar{1}\bar{1}0]$ . The third one,  $[\bar{1}\bar{1}0]$ , is along the texture axis; however, glide on this plane is impossible because of the small thickness of our simulation cell in the texture direction. Another, analogous set of glide directions,  $[01\bar{1}]$ , and  $[10\bar{1}]$ , exists for glide on the  $(111)$  plane. These combinations enable a number of cross-slip formations between the  $(11\bar{1})$  and  $(111)$  glide planes (such as the Lomer-Cottrell locks in grain 3 in Fig. 2 and in configuration (10) in Fig. 3).

Using the above terminology, we can now characterize the dislocation reactions involved in the deformation-twinning processes seen in our simulations. We first analyze the relatively simple structure resulting from the overlap of two ISFs associated with two extended dislocations, DA and DB, dissociated according to the reactions (3) and (4) (see formation 7a in Fig. 3). Fig. 9(a) and (b) provide projections of this formation parallel and perpendicular to the texture direction. Fig. 9(a) reveals the deviations from the perfect-crystal, ABC, stacking arrangement resulting from the overlap of the extended dislocation DA (the upper one) with DB (the lower one). As indicated by the arrows, the (pure-edge) partial on the left produces a shift in the stacking sequence, forming the ISF, with stacking ABABC. The pure-edge partial in the center produces an additional shift, transforming the ISF into an ESF, with stacking ABACA. Finally, the perfect-crystal stacking is recovered by the two partials on the right, one mixed  $-30^\circ$  partial and one pure-edge partial, combined into a D-Shockley partial.

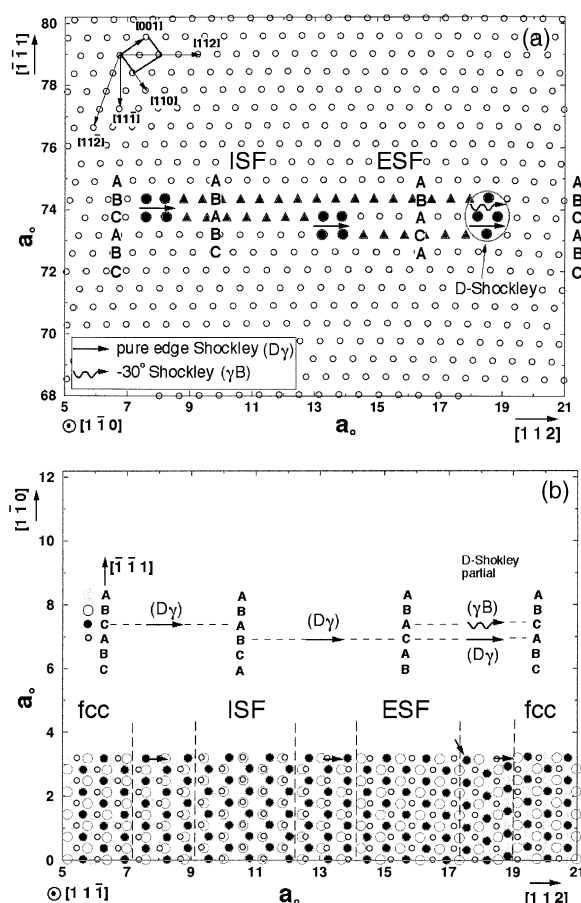


Fig. 9. Atomic structure of configuration 7a in Fig. 3, illustrating how two overlapping ISFs produce an ESF. The ABC stacking sequences of the (111) planes sketched in the insets characterize the types of stacking faults and dislocations involved. All positions are given in units of the zero-temperature lattice parameter,  $a_0$ . Common-neighbor analysis distinguishes atoms in fcc (o), hcp ( $\blacktriangle$ ) and defected ( $\bullet$ ) surroundings. (a) View down the  $[1\bar{1}0]$  textured axis. The motifs of the two  $[110]$  stacking planes, together with the relevant crystallographic directions, are given for clarity. (b) Edge-on view down the  $[11\bar{1}]$  direction of four  $(11\bar{1})$  planes (labeled in the inset, in the same  $[\bar{1}\bar{1}1]$  projection as in (a)), revealing the atomic structure of the partial dislocations involved in the formation. The relative shifts of the atom positions in the dislocation cores (shown as small arrows at the surface of the layered structure) give the actual Burgers vectors.

The partial-dislocation *core* structures resulting from this overlap are best revealed in the projection in (b), along  $[11\bar{1}]$ , because all the Burgers vectors lie in the  $(11\bar{1})$  plane. To visualize these Burgers

vectors, we show only the atom positions in four  $(11\bar{1})$  planes (labeled in the inset, in the same  $[\bar{1}\bar{1}1]$  projection as in (a)). Of particular interest are the relative shifts of the third and fourth atomic layers in this inset (atoms depicted as small full and open circles); we note that in the  $[11\bar{1}]$  projection of the actual atom positions in (b), these form the top two  $(11\bar{1})$  planes. The relative shifts of these atom positions in the dislocation cores (shown as small arrows) give the actual Burgers vectors.

Of particular interest is the formation of the D-Shockley partial on the right which terminates the ESF and restores the perfect fcc lattice. This partial results from the overlap of the cores of the two mixed partials  $\gamma A$  and  $\gamma B$  (see Eqs. (3) and (4)) with *opposite* screw components and *equal* edge components (see inset). Their vector sum gives the Burgers vector of the  $1/6[112]$   $D\gamma$  partial, in the fourth stacking layer in Fig. 9(b). The implication of this observation is that, in the process of stacking-fault overlap, a D-Shockley partial can *only* be formed from two approaching partials of different types (i.e.,  $D\gamma$ ,  $\gamma A$  or  $\gamma B$ ). This is consistent with the analysis by Hirth and Hoagland [37] that a D-Shockley partial in Al is formed of two S-Shockley partials on parallel, neighboring glide planes, but having different orientations of their Burgers vectors. If the two partials are of the same type, then they cannot combine into a D-Shockley partial; instead, they repel and remain separated at a certain distance from each other. This explains our observations that D-Shockley partials are not always formed in the process of stacking-fault overlap. For example, the two partials in the left half in Fig. 9(a) remain separated because both of them are pure-edge partials, unlike the two on the right side which combine.

When a third intrinsically dissociated dislocation joins the above formation, a *two-layer* microtwin is produced (see, e.g., configuration 7b in Fig. 3). The atomic structure of this formation is analyzed in Fig. 10, in a manner analogous to Fig. 9(a). In this particular case, the three initial extended dislocations involve two of type DA and one of type DB (see Fig. 8); they are dissociated according to the reaction equations:

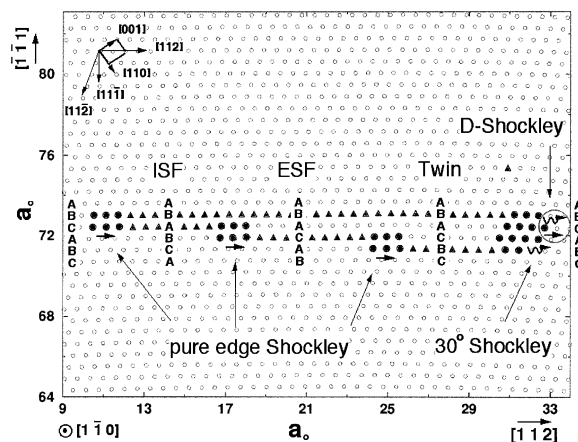


Fig. 10. View down the  $[1\bar{1}0]$  texture axis of the atomic structure of three overlapping ISFs producing the two-layer twin configuration 7b in Fig. 3, with a complex core structure on the right consisting of a D-Shockley and an S-Shockley partial. The symbols are identical to those in Fig. 9(a).



Starting from the top of Fig. 10, the subscripts indicate the particular dissociated dislocation. Since all three partials in the left portion of the microtwin are of the same pure-edge type,  $D\gamma$ , they remain separated; by contrast, the remaining three partials (two  $30^\circ$  partials,  $\gamma A$ , and one pure-edge type,  $D\gamma$ ) combine to form a complex core structure consisting of a D-Shockley and an S-Shockley partial which, as shown below, can lead to the formation of an incoherent-twin boundary.

When yet another intrinsically dissociated dislocation joins the above formation, a *three-layer* microtwin is produced (see, e.g., configuration (3) in Fig. 6(g)). Its atomic structure is analyzed in Fig. 11, in a manner completely analogous to Fig. 9(a) and 10. Our analysis reveals that the structure of the incoherent twin boundary which terminates the twin again consists of a series of partials of alternating types, here grouped into two D-Shockley partials. We note, however, that by contrast with the (horizontal) coherent twin boundary, the plane of this  $[1\bar{1}0]$   $70.5^\circ$  tilt GB is inclined, by the angle  $\alpha$ , with respect to the  $(11\bar{1})$  mirror planes in Fig. 11.

The above comparison of the two-layer and

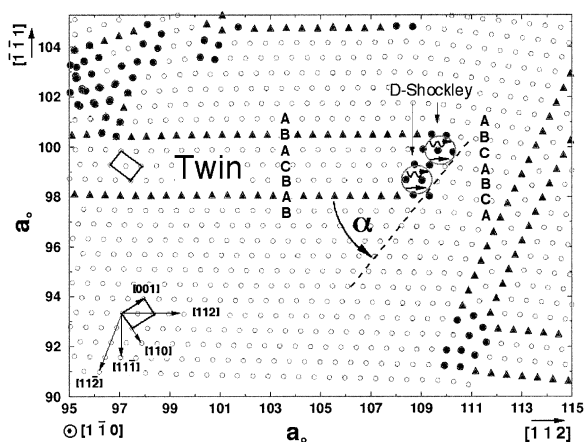


Fig. 11. View down the  $[1\bar{1}0]$  texture axis of the atomic structure of a glissile incoherent twin boundary similar to that in configuration (3) in Fig. 6(g), revealing a core structure composed of two D-Shockley partials.  $\alpha$  is the inclination angle of this GB with respect to the  $(11\bar{1})$  mirror planes in the horizontal coherent twin boundaries. The symbols are the same as in Fig. 9 (a).

three-layer microtwins (see Figs. 10 and 11) reveals that, in general, the inclination of the terminating incoherent twin is determined by the particular combination of the twinning dislocations which form the incoherent twin boundary. Specifically, if the incoherent twin consists of a series of D-Shockley partials (e.g., in the right halves of Fig. 9(a), 10 and 11), the inclination relative to the mirror plane is close to  $90^\circ$  (see, e.g., Fig. 11). By contrast, in an incoherent twin consisting only of one type of S-Shockley partials (such as in the left halves of Fig. 9(a) and (10)), then their cores repel each other, causing the inclination to be rather small (see also Ref. [28]). Other examples of such only slightly inclined incoherent twins are the twin interfaces of the lenticular twin  $\tau_2$  in Fig. 2 and in the heterogeneously twinned configuration labeled 1–5 in Fig. 3.

An incoherent twin boundary may also contain dislocations other than Shockley partials. For example, the atomic structure of configuration (6) in Fig. 6(h) shown in Fig. 12 reveals the presence of a Frank partial dislocation in the terminating incoherent twin boundary of this six-layer twin lamella. In addition to the series of D-Shockley partials seen in Figs. 9–11, this boundary contains

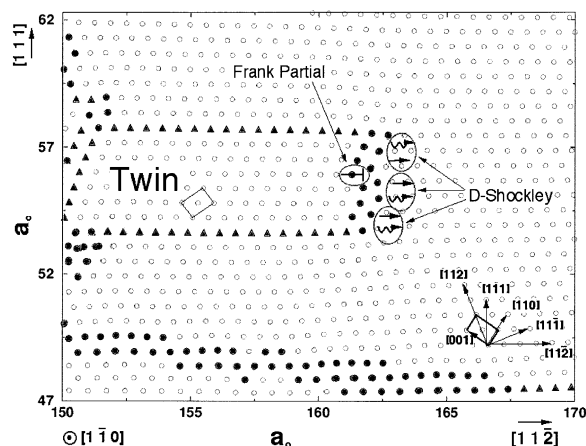


Fig. 12. View down the  $[1\bar{1}0]$  texture axis of the atomic structure of the sessile incoherent-twin boundary in configuration (6) in Fig. 6(h), revealing the presence of a Frank-partial 'defect' in the structure of the incoherent twin. The symbols are the same as in Fig. 9(a).

in its middle a  $1/3[11\bar{1}]$  Frank partial dislocation [29]. As discussed below, this 'defect' in the structure of the incoherent twin strongly affects its mobility.

The mobility of the various types of incoherent twin boundaries considered above is governed by the mobility of the dislocations in their structure. Since all Shockley partials are glissile dislocations (i.e., they readily glide on  $\{111\}$  planes), incoherent twin boundaries composed solely of Shockley partials are 'glissile incoherent twins', with a high mobility in the twinning direction. By contrast, if the incoherent-twin structure includes at least one sessile dislocation, such as a Frank partial (see Fig. 12), it exhibits a rather low mobility because the sessile dislocation pins the twin boundary ('sessile incoherent twin').

The fact that the mobilities of deformation-twin lamellae depend strongly on the mobility of their incoherent-twin boundaries is nicely seen from the comparison of the motions of the two twin lamellae labeled (3) and (6) in Fig. 6(g) and (h). We note that the resolved shear stresses on the two structures are approximately equal. However, since lamella (3) is headed by a glissile twin boundary of the type analyzed in Fig. 11, it propagates very quickly through the grain: the lamella was nucleated only about 8 ps before snapshot (g) was

taken; then, in and the snapshot in (h), taken only 20 ps after (g), its front has already moved out of view towards the grain interior. Detailed analysis yields a propagation velocity of  $\sim 900$  m/s, i.e., well below the speed of sound in the [100] direction for our potential of 3664 m/s [17], but significantly higher than the gliding velocity of an intrinsically dissociated dislocation of  $\sim 500$  m/s under the same resolved shear stress [14].

By contrast, the lamella labeled (6) in Fig. 6(h) is headed by the sessile incoherent twin boundary containing a Frank partial analyzed in Fig. 12. The fact that this lamella is seen on all nine snapshots in Fig. 6 reveals that it has moved very little during the entire time period of  $\sim 50$  ps. In fact, its front containing the Frank partial has moved by only about 0.5 nm during  $\sim 50$  ps, yielding a propagation velocity of  $\sim 10$  m/s. This comparison confirms that the mobility of a glissile incoherent twin boundary can be orders of magnitude higher than that of its sessile counterpart.

The different mobilities of these two types of deformation-twin lamellae can be expected to strongly affect their possible roles during any recovery processes. To test this assertion, the external load was switched off at the moment at which the snapshot in Fig. 6(g) was taken while the simulation was continued. This simulation revealed the immediate onset of a recovery process involving lamella (3): its fast propagation stops virtually immediately (i.e., in  $< 1$  ps) and is reversed until,  $\sim 20$  ps later, it is completely re-absorbed by the GB from where it had been nucleated. By contrast, the position of the twin lamella (6) remained entirely unchanged, its sessile incoherent twin boundary preventing the onset of a recovery process.

## 5. Discussion and conclusions

Our simulations of highly idealized columnar microstructures with a grain size of less than  $0.1 \mu\text{m}$  reveal a competition between dislocation slip and deformation twinning in the room-temperature deformation behavior of nanocrystalline Al. Particularly during the later stages of the deformation, when the dislocation density nucleated from the

GBs is high and the grain interiors are more or less saturated with dislocations, stacking faults and dislocation obstacles, such as Lomer-Cottrell locks, we observe a prolific tendency for deformation twinning. Moreover, the complex deformation substructures dynamically formed from dislocations, stacking faults and already nucleated microtwins can evolve into a new grain, and thus initiate recrystallization.

The propensity for deformation twinning observed in our simulations is surprising, given that (i) the well-known pole mechanism [8,9] cannot operated for such a small grain size and (ii) the process has never been observed in coarse-grained Al, not even in shock-wave experiments [7]. We note, however, that MD simulations are inherently limited to very high strain rates (of typically  $> 10^7 \text{ s}^{-1}$ ), which might prevent the onset of recovery and thus give the appearance of more twinning than would actually be observed at lower strain rates. However, the fact that our simulations are carried out under much lower—and uniform—stresses than are present in the shock-wave experiments, suggests that the observed twinning cannot be simply attributed to the high strain rates in our simulations (of  $\sim 10^8 \text{ s}^{-1}$ ). It therefore appears that this propensity for twinning for a nanocrystalline grain size may, in fact, be a real effect, arising in part from the prolific nucleation of partial dislocations from the dense network of GBs and grain junctions in these materials.

In agreement with experimental observations for coarse-grained fcc metals, our simulations reveal both the heterogeneous and homogeneous mechanisms for the nucleation of microtwins. The heterogeneous nucleation from the GBs or grain junctions involves the successive emission of partial dislocations onto neighboring slip planes; by contrast, the homogeneous nucleation in the grain interiors can occur either via the mechanisms of stacking-fault overlap or by partial-dislocation breakaway. Interestingly, the heterogeneous mechanism is very similar to the mechanism observed earlier [14] for the nucleation of complete extended dislocations from the GBs or grain junctions. The nucleation of an extended dislocation involves the consecutive emission of two partials of different

types onto the same glide plane, thus terminating the trailing stacking fault created by the first partial. By contrast, the twin-nucleation process requires that the second partial is of the same type as is the first one, and emitted onto a neighboring slip plane (see also processes 1–5 in Fig. 3).

For a grain size of 45 nm, our simulations yield typical dislocation densities of about  $10^{15} \text{ m}^{-2}$  at ~12% strain. Such high densities are not unusual for nanocrystalline fcc metals, as evidenced by measured dislocation densities of  $\sim 10^{14} \text{ m}^{-2}$  in ultrafine-grained Cu and Ni with grain sizes of 107 and 114 nm, respectively, produced by severe plastic deformation [39]. The present work suggests that the high density of partials and extended dislocations leads to a very high stacking-fault concentration which can trigger the formation of twins as a result of recovery processes. That such high densities of stacking faults, indeed, exist in nanocrystalline materials has been confirmed by X-ray [39] and TEM experiments [39–42].

The question remains as to what fraction of the total plastic strain in a nanocrystalline material is actually produced by twinning. Although in fcc metals the twinning systems are different from the slip systems, they are equal in number (each {111} plane has three {112} twin and three {110} slip directions). This is why in coarse-grained materials twinning increases the flexibility of the grain to respond to deformation. Our simulations offer no reason why the same should not also be true for nanocrystalline materials. Moreover, as reviewed in the Introduction, it is also known that in coarse-grained materials dislocations piling up against twin boundaries produce a yield stress in accordance with the Hall-Petch relation [9]. If this were also valid for nanocrystalline materials, it might possibly explain the observed Hall-Petch hardening down to very small grain sizes (of ~20 nm) [43]. Given that the usual dislocation pile-up model cannot explain this behavior for such small grain sizes [14,44], twinning may well provide a more viable explanation for these observations.

Finally, we should comment on the inherent limitations in the observed deformation behavior arising from the columnar simulation geometry chosen here. While enabling us to probe the deformation behavior in a considerably larger grain-size

regime than studied before [19–21], this geometry has the consequence that the microstructure is effectively two-dimensional, consisting of infinitely long cylindrical grains. This in itself is not an entirely unphysical situation, given that such columnar 2d microstructures are commonly observed in thin films, albeit usually attached to a substrate. However, such a columnar geometry limits the dislocations emitted from the GBs to be parallel to each other and to the GBs; moreover, due to the rather short periodic repeat length of the simulation cell in the  $\langle 110 \rangle$  texture direction, these dislocations are always straight, i.e., free of kinks.

In a columnar thin film with a  $\langle 110 \rangle$  texture axis, only four of the 12 slip systems present in a 3d grain structure can be activated during the deformation. [14] Each columnar grain therefore contains only two active slip planes rather than the four in a 3d grain microstructure. In practice, two independent slip systems are sufficient to accommodate any deformation in the  $x$ - $y$  plane; however, usually only one of these (known as the primary slip system) is active during plastic deformation. Also, suppression of kinks on the dislocation lines will suppress certain types of dislocation dynamics and modify the dislocation-nucleation process from the GBs, giving rise to some hardening of the material and an increase in the dislocation-nucleation stress, as evidenced by the extremely high threshold stress of 2.3 GPa observed for this simulation geometry [14]. In spite of these limitations, as critical test cases our simulations correctly reproduce key elementary dislocation processes, such as the structure of dissociated dislocations in fcc metals, Lomer-Cottrell lock formation and the mechanism for mechanical twinning.

In summary, the main difference between our observations and the known mechanisms for deformation twinning in coarse-grained materials appears to arise from the absence of the pole mechanism in the nanocrystalline material and the high density of GB sources. As described in the Introduction, the pole mechanism cannot operate because the twinning stress,  $\sigma_t \sim d^{-1}$ , is too high for a nanocrystalline grain size [9]. This inability of the pole mechanism to provide sources for defor-

mation twinning mirrors the inability of Frank-Read sources to provide dislocations for slip deformation in materials with a submicron grain size.

## Acknowledgements

V.Y., D.W. and S.R.P. are supported by the US Department of Energy, BES-Materials Science under contract W-31-109-Eng-38. V.Y. is also grateful for support from the DOE/BES Computational Materials Science Network (CMSN). We are grateful for grants of computer time on the Cray-T3E at the John-von-Neumann-Institute for Computing in Jülich, Germany and on the Chiba City Linux cluster at ANL.

## References

- [1] Christian JW, Mahajan S. *Prog Mater Sci* 1995;39:1.
- [2] Rohatgi A, Vecchio KS, Gray III TG. *Met and Mat Trans* 2001;32A:135.
- [3] Venables JA. In: Reed-Hill RE, Hirth JP, Rogers HC, editors. *Deformation twinning*. New York: Gordon and Breach; 1964. p. 7.
- [4] Cottrell AH, Bilby BA. *Phil Mag* 1951;42:573.
- [5] Hull D. In: Reed-Hill RE, Hirth JP, Rogers HC, editors. *Deformation twinning*. New York: Gordon and Breach; 1964. p. 121.
- [6] Blewitt TH, Coltman RR, Redman JK. *J Appl Phys* 1957;28:651.
- [7] Gray III TG. *Acta Met* 1988;36:1745.
- [8] Venables JA. *Phil Mag* 1961;6:379.
- [9] Venables JA. *J Phys Chem Solids* 1964;25:693.
- [10] El-Danaf E, Kalidindi SR, Doherty RD. *Met and Mat Trans* 1999;30A:1223.
- [11] Hu SY, Ludwig M, Kizler P, Schmauder S. *Modeling Simul Mater Sci Eng* 1998;6:567.
- [12] Pinsook U, Ackland GJ. *Phys Rev B* 2000;62:5427.
- [13] Lill JV, Broughton JQ. *Phys Rev B* 2001;63:144102.
- [14] Yamakov V, Wolf D, Salazar M, Phillpot SR, Gleiter H. *Acta Mater* 2001;49:2713.
- [15] Yamakov V, Wolf D, Phillpot SR, Mukherjee AK, Gleiter H. *Nature Materials* 2002;1:45.
- [16] Parrinello M, Rahman A. *Phys Rev Lett* 1980;45:1196.
- [17] Ercolessi F, Adams JB. *Europhys Lett* 1994;26:583.
- [18] Noonan JR, Davis HL. *Phys Rev B* 1984;29:4349.
- [19] Schiotz J, Di Tolla FD, Jacobsen KW. *Nature* 1998;39:561.
- [20] Schiotz J, Di Tolla FD, Jacobsen KW. *Phys Rev B* 1999;60:11971.
- [21] Swygenhoven HV, Spaczer M, Caro A. *Acta Mater* 1999;47:3117.
- [22] Jonsson H, Andersen HC. *Phys Rev Lett* 1988;60:2295.
- [23] Clarke AS, Jonsson H. *Phys Rev E* 1993;47:3975.
- [24] Yamakov V, Wolf D, Phillpot SR, Gleiter H. *Acta Mater* 2002;50:61.
- [25] Frenkel J. *Zeit Phys* 1926;37:572.
- [26] Gouldstone A, Koh H-J, Zeng K-Y, Giannakopoulos AE, Suresh S. *Acta Mater* 2000;48:2277.
- [27] Gouldstone A, Van Vliet KJ, Suresh S. *Nature* 2001;411:656.
- [28] Hirth JP, Lothe J. *Theory of dislocations*. John Wiley & Sons, Inc, 1991.
- [29] Weertman J, Weertman JR. *Elementary dislocation theory*. New York, Oxford: Oxford University Press, 1992.
- [30] Bulatov V, Abraham FF, Kubin L, Devincere B, Yip S. *Nature* 1998;391:669.
- [31] Zhou SJ, Preston DL, Lomdahl PS, Beazley DM. *Science* 1998;279:1525.
- [32] Ashby MF, Harper E. *Harvard Rept. Sept*. Cambridge, MA: Harvard Univ, 1967.
- [33] Gleiter H. In: Christian JW, Haasen P, Massalski TB, editors. *Progress in materials science, Chalmers anniversary volume*. Oxford: Pergamon Press; 1981. p. 17-2.
- [34] Fullman RL. *J Appl Phys* 1950;21:1069.
- [35] Fullman RL. *J Appl Phys* 1951;22:456.
- [36] Fullman RL, Fisher JC. *J Appl Phys* 1951;22:1350.
- [37] Hirth JP, Hoagland RG. *Phil Mag A* 1998;78:529.
- [38] Thompson N. *Proc Phys Soc* 1953;66B:481.
- [39] Islamgaliev RK, Chmelik F, Kuzel R. *Mat Sci Eng* 1997;335:A234–6.
- [40] Wang ZL, Dai Z, Sun S. *Adv Mater* 2000;12:1944.
- [41] Furuya K, Mitsuishi K, Ishikawa N, Allen CW. *Mat Sci Eng* 2000;A285:85.
- [42] Straub WM, Gessmann T, Sigle W, Phillipp F, Seeger A, Schaefer H-E. *NanoStruct Mater* 1995;6:571.
- [43] Koch CC, Suryanarayana C. In: Li JCM, editor. *Microstructure and properties of materials, 2*. Singapore: World Scientific Publishing; 2000. p. 359–403.
- [44] Wang N, Wang Z, Aust KT, Erb U. *Acta Metall Mater* 1995;43:519.